


Voltage-Driven High-Speed Skyrmion Motion in a Skyrmion-Shift Device

Yizheng Liu,¹ Na Lei,^{1,*} Chengxiang Wang,¹ Xichao Zhang,² Wang Kang,¹ Daoqian Zhu,¹ Yan Zhou,² Xiaoxi Liu,³ Youguang Zhang,¹ and Weisheng Zhao^{1,†}

¹*Fert Beijing Institute, BDBC, School of Microelectronics, Beihang University, Beijing 100191, China*

²*School of Science and Engineering, The Chinese University of Hong Kong, Shenzhen, Guangdong 518172, China*

³*Department of Electrical and Computer Engineering, Shinshu University, 4-17-1 Wakasato, Nagano 380-8553, Japan*

 (Received 3 April 2018; revised manuscript received 4 December 2018; published 3 January 2019)

Magnetic skyrmions are promising information carriers for building future high-density and high-speed spintronic devices. However, to achieve a current-driven high-speed skyrmion motion, the required driving-current density is usually very large, which could be energy inefficient and even destroy the device due to Joule heating. The mechanism of voltage-driven skyrmion motion through equidistant identical electrodes on a uniformly thick nanowire is studied. The high-speed skyrmion motion is realized by utilizing a voltage shift, and the average skyrmion velocity reaches up to 259 m/s under a 0.45-V applied voltage. In comparison with the widely studied vertical current-driven model, the energy dissipation is three orders of magnitude lower in our voltage-driven model for the same speed motion of skyrmions. Our approach uncovers valuable opportunities for building skyrmion racetrack memories and logic devices with both ultra-low power consumption and ultra-high processing speed, which are appealing features for future spintronic applications.

DOI: [10.1103/PhysRevApplied.11.014004](https://doi.org/10.1103/PhysRevApplied.11.014004)

I. INTRODUCTION

Magnetic skyrmions show great potential as information carriers in spin memory and logic devices, because they have a number of merits including small size, low-driving-current density, and topological stability [1–7]. Manipulations of magnetic skyrmions, including creation, motion, and annihilation, have been intensively studied both theoretically [8–15] and experimentally [16–25]. Electric current is preferred to manipulate the skyrmion [26–30], especially for skyrmion motion [31–38]. The threshold current density to drive skyrmions is around 10^6 A m^{-2} , which is over five orders of magnitude lower than that of conventional domain walls (DWs) [26]. However, a large-driving-current density is required to achieve high-speed skyrmion motion for fast information processing, which would result in a significant amount of Joule heating [1,36] and induce instability of the devices [3,12]. In addition, for current-driven skyrmion motion, geometric patterns [39,40] or additional electric gates [41] are usually attached to pin the skyrmion for realizing addressable control, which increases the cost of operating energy and limits the maximum speed of skyrmion motion. For these reasons, more efficient and reliable means for controlling high-speed skyrmion motion are required.

Instead of a current-driven approach, various approaches, such as spin wave [9,19], magnetic-field gradient [14], and many more have been proposed for driving skyrmion motion. Most of these methods lack practical convenience in integrated electrical circuit applications and may not be energy efficient for commercial use.

The electric field or voltage has been proposed to be an energy-efficient method to manipulate magnetism [42,43] and has been progressively applied to the development of skyrmion-based applications [25,44,45]. Very recently, a voltage-controlled magnetic anisotropy (VCMA) gradient model to drive skyrmions was numerically shown by Wang *et al.* [46], in which a wedged insulating layer was used to generate the magnetic anisotropy gradient, which can avoid the Joule heating effect. In the last part of their work, the discrete gate electrodes instead of a single entire gate electrode was proposed for the long distance of skyrmion motion. Such a design of the discrete gate electrodes is promising for skyrmionics device applications. However, in order to develop real devices, a prerequisite is the study of the size and deformation of the skyrmion, and the analytical model is highly required to fit the application criteria of practical and reliable high-speed skyrmion motion.

In this work, a series of equidistant identical electrodes on a nanowire with a uniform thickness structure is studied for high-speed skyrmion motion. A voltage-induced

*na.lei@buaa.edu.cn

†weisheng.zhao@buaa.edu.cn

energy barrier and energy well on the sides of the skyrmion drive its directional motion to the addressable position along the nanowire. An analytical model is developed to describe the spin texture in the skyrmion profile passing through an energy step induced by VCMA. To realize high-speed data delivery, parameters are optimized with a solution is proposed for long-range skyrmion motion, including the effects of the size and deformation of skyrmions. With that optimization, the maximum velocity reaches 259 m/s when a 0.45-V voltage is applied. Under a 0.15-V voltage, only 8.4 aJ is consumed for one shift of a single skyrmion with an average velocity of 100 m/s. Our method shows great advantages in the potential application of skyrmion-based racetrack memory or spin logic devices.

II. SIMULATION RESULTS AND DISCUSSION

A. Model

The device structure is shown in Fig. 1(a). Skyrmions move in a magnetic nanowire of 100-nm width on which contacts with uniform width and equidistance are deposited as voltage gates. Numerical calculations are performed using the Object Oriented Micromagnetic Framework (OOMMF), which allows magnetization dynamics simulation by solving the Landau-Lifshitz-Gilbert equation, written as

$$\frac{\partial \mathbf{m}}{\partial t} = -\gamma_0 (\mathbf{m} \times \mathbf{h}_{\text{eff}}) + \alpha \left(\mathbf{m} \times \frac{\partial \mathbf{m}}{\partial t} \right), \quad (1)$$

where \mathbf{m} is the reduced magnetization, γ_0 is the gyromagnetic ratio, and \mathbf{h}_{eff} is the effective field. Magnetic parameters based on typical Co-Fe-B/MgO perpendicular magnetic anisotropy (PMA) systems are used to model the magnetic nanowire [47,48]: the PMA constant is $K = 310\text{--}360$ kJ/m³, the Dzyaloshinskii-Moriya interaction (DMI) constant is $D = 0.9\text{--}1.2$ mJ/m², the saturation magnetization is $M_S = 6 \times 10^5$ A/m, the exchange coefficient is $A_{\text{ex}} = 1.12 \times 10^{-11}$ J/m, and the Gilbert damping constant is $\alpha = 0.3, 0.1, \text{ or } 0.02$. Due to the skyrmion Hall effect, the skyrmion speed can reach 30 m/s before its annihilation at the edge in the nanowire with uniform anisotropy. Thus, the higher anisotropic constant K_{edge} at the edge is considered to avoid the annihilation of skyrmions. Doubling the anisotropy at the edge can sufficiently suppress the skyrmion annihilation [49]. Different thicknesses or high- K materials at the edge have been proposed to obtain a high anisotropic edge [50,51]. Considering the experimental feasibility, light ion irradiation can also be used to locally achieve higher anisotropy at the edge, which has been reported to enhance the magnetic anisotropy after film deposition [52]. On the other hand, modification of magnetic properties in a nanowire can also be realized by using thermal diffusion of elements [53]. In the following, the higher anisotropy is set at the edge as $K_{\text{edge}} = 3$ MJ/m³ to simplify the simulation.

Due to the VCMA effect, voltages applied on contacts will induce local anisotropy changes [54–56]. In our simulation, we set the VCMA coefficient ξ as 100 fJ/Vm, which has been experimentally demonstrated in an

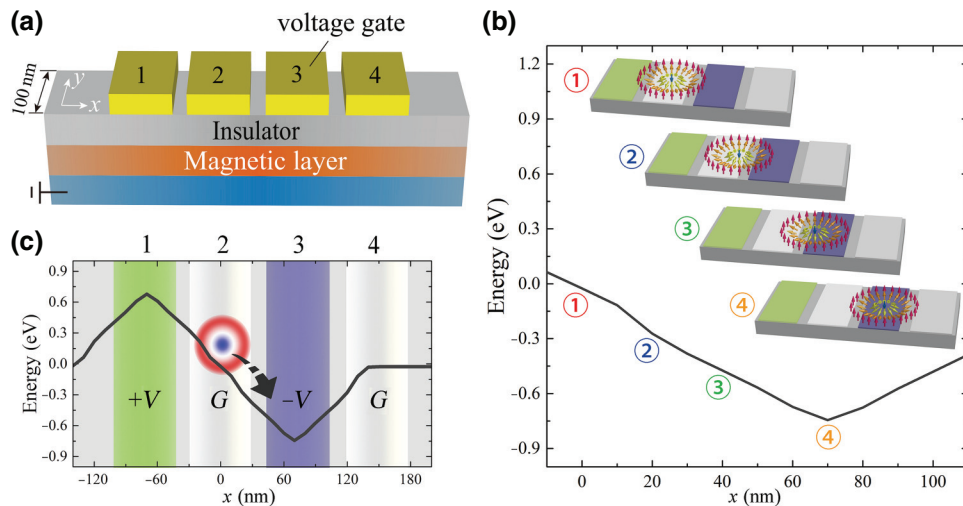


FIG. 1. (a) Sketch of the proposed device structure. Uniform width contacts on a 100-nm-wide nanowire serve as voltage gates with equidistant spacing. The insulating layer acts as a dielectric layer for the VCMA effect and the magnetic layer is for the generation of skyrmions. The nanowire is along the x axis. (b) Different skyrmion locations and the corresponding total energy of the system. The energy profile is continuously evaluated when skyrmions are located at different positions along the x axis. (c) The variation of the total energy when a skyrmion is centered at different locations along a nanowire under voltages $+V$, ground (G), $-V$, and ground (G) applied to contacts 1 to 4, successively. The potential barrier and well are formed at contacts 1 and 3, the skyrmion located at contact 2 falls into the energy well at contact 3. The potential well is 0.98 eV when a 0.3-V voltage is applied.

Ir/Co-Fe-B/MgO system [57] and a Ta/Co-Fe-B/MgO system [58]. Note that the energy variation is linearly proportional to the VCMA coefficient ξ , thus a larger ξ will lower the applied voltage to achieve the same energy profile. Recently, VCMA coefficients ξ up to 290 and 370 fJ/Vm have been reported in experiments on a Cr/Fe/MgO system [59,60]. The typical thickness of the MgO layer is 1 nm and the applied voltage is assumed to be 0.3 V. Under these conditions, an electric field of 0.3 V/nm in the MgO layer induces a change of 30 kJ/m³ in the magnetic anisotropy constant K , which is about a 9.5% anisotropy change [61] (the typical dielectric breakdown field strength of MgO is about 2.4 V/nm [62,63]). In order to drive a skyrmion, positive and negative voltages are applied to contacts 1 and 3, respectively, while contacts 2 and 4 are connected to the ground. An analytical model is developed to describe the energy evolution when different spin textures cross a step-like anisotropy profile, including a square-shaped domain, circular-shaped domain, and skyrmions, based on $E = -\mathbf{m} \cdot \mathbf{H}$ (see Appendix A). The calculation results indicate that a spin texture with finite size will generate an energy gradient when it passes through a step-like anisotropy field induced by VCMA. Benefitting from the finite size of the skyrmion spin texture, the total energy continually evolves with a skyrmion located at different positions along the nanowire with voltage applied, as shown in Figs. 1(b) and 1(c). Moreover, the energy gradient width is closely linked with the skyrmion size (see Appendix B). In case the skyrmion radius, R_{sk} (radius of the $m_z = 0$ contour) is negligible compared with the contact width and a step-like energy platform is expected [46]. In the case where the skyrmion diameter is equivalent to the contact width, a continuous energy gradient is formed, as shown by the black curve in Fig. 1(c). The potential barrier and well of 0.98 eV on the left and right sides of a skyrmion centered at contact 2 are achieved. Then the skyrmion shifts to contact 3, the potential well, realizing a voltage-driven shift of the magnetic skyrmion.

B. Voltage-driven skyrmion dynamics

For the analysis of skyrmion dynamics, the Thiele equation is generally used with an assumption of rigid skyrmions. However, in our case, the skyrmion deformation is non-negligible, thus the Thiele equation can just serve for qualitative analysis. In consideration of the driving force from the energy gradient \mathbf{F}_g and repulsive force from the edge \mathbf{F}_e , the equation is written as [28,64,65]

$$\mathbf{G} \times \mathbf{v} - \alpha \mathbf{D} \times \mathbf{v} + \mathbf{F}_g + \mathbf{F}_e = 0, \quad (2)$$

where \mathbf{v} is the instantaneous velocity of the skyrmion. \mathbf{G} is the total gyromagnetic coupling vector, which only has a z component $G_z = \int_{\text{sk}} dr^2 \mathbf{m} \cdot (\partial_x \mathbf{m} \times \partial_y \mathbf{m}) = 4\pi N_{\text{sk}}$ (N_{sk} is the skyrmion number, and sk stands for the skyrmion

region). \mathbf{D} is the dissipative tensor, whose elements are given by $D_0 = D_{xx} = D_{yy} = \int_{\text{sk}} dr^2 \partial_x \mathbf{m} \partial_y \mathbf{m}$. \mathbf{F}_g is only the function of x , which can be expressed as $F_g(x) = \partial_x E_{\text{ani}}(x)$ (See Appendix A). \mathbf{F}_e is perpendicular to the nanowire edge, thus it is along the y axis. The analytical solution for the instantaneous velocity can be expressed as

$$\begin{pmatrix} v_x \\ v_y \end{pmatrix} = \frac{1}{G_z^2 + \alpha^2 D_0^2} \begin{pmatrix} F_g \alpha D_0 - F_e G_z \\ F_g G_z + F_e \alpha D_0 \end{pmatrix}, \quad (3)$$

where v_x and v_y are the longitudinal and transverse components of instantaneous velocity, respectively.

As shown in Fig. 2(a), a skyrmion is driven toward the right contact (energy well) when the voltage pulses are applied. The skyrmion is not moving in a straight line along the nanowire as its trajectory (black dashed line) exhibits a noticeable transverse drift in voltage-driven motion. The corresponding longitudinal and transverse components v_x and v_y are plotted in Fig. 2(b), respectively, where v_x is much larger than v_y . The voltage driving force and the edge repulsive force contribute to both v_x and v_y , which are inversely proportional to the damping constant α . The transverse velocity v_y causes the skyrmion

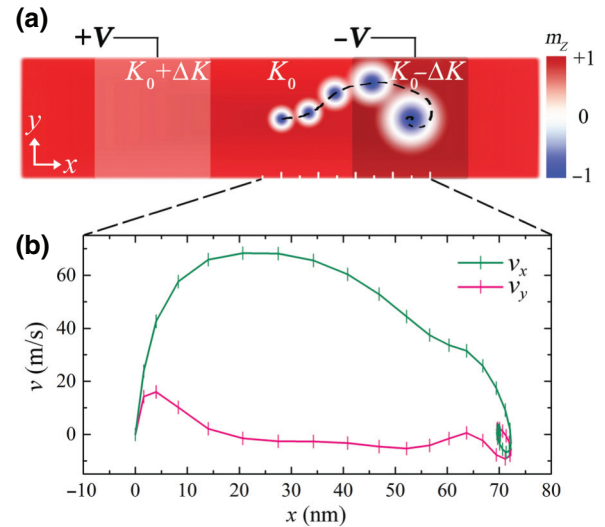


FIG. 2. (a) Top view of the nanowire and typical trajectory of the skyrmion shift. $+V$ and $-V$ are applied to the left and the right contacts, respectively, to create a positive and a negative anisotropy constant change ΔK , respectively. The regions with red color (blue color) represent $m_z = +1$ ($m_z = -1$) of the magnetic layer. The skyrmion size increases at different locations during one shift. Note that the skyrmion size is compressed in order to clearly show the evolution of its size and trajectory. (b) Evolution of instantaneous velocity during the shift. v_x and v_y are the longitudinal and transverse components of velocity obtained with anisotropic constant $K = 360$ kJ/m³ and Dzyaloshinskii-Moriya interaction constant $D = 1.2$ mJ/m².

Hall effect, resulting in a transverse drift in the voltage-driven motion of a skyrmion. To avoid the annihilation of skyrmions, the anisotropic constant K is set higher at the edge [51].

Furthermore, an obvious skyrmion size change can be observed during its shift, which is consistent with the theoretical expression of skyrmion radius [8]

$$R_{\text{sk}} \approx \frac{\Delta}{\sqrt{2(1 - D/D_c)}}, \quad (4)$$

where $\Delta = \sqrt{A/K}$ and $D_c = 4\sqrt{AK}/\pi$. In our model, as the energy well is centered at the zone with decreased K , the skyrmion radius should increase when it moves toward the energy well.

One important feature of the voltage-driven motion is that the skyrmion will always overshoot the center of an energy well and process for a while. The procession is very sensitive to the damping constant α , and becomes extremely time-consuming at lower α . It occupies only 0.05 ns in a 1.5-ns shift under $\alpha = 0.3$, but occupies 14 ns in a 15-ns shift with $\alpha = 0.02$. This leads to a large reduction in the average velocity for a single shift.

C. Long-range skyrmion motion

In skyrmion-based memory and logic devices, long-range skyrmion motion is demanded. To enhance the efficiency in long-range skyrmion motion, the relaxation process owing to the overshoot can be suppressed or avoided. One solution is to switch the voltages once skyrmions cross the centers of the contacts, so that the procession is skipped and skyrmions continue to move directly to the designated contact (see Fig. 3).

As a demonstration, one motion containing four single shifts in Fig. 3 exhibits the behavior of long-range skyrmion motion driven by voltage. A long-range motion can be divided into three steps. That is, the first shift from t_0 to t_1 , the second from t_1 to t_3 , and the last shift from t_3 to t_4 . The average velocities of each shift follow the relationship $v_1 \approx v_2 > v_0 > v_3$ (shifts in the middle steps exhibit a similar velocity). For example, with the parameters given in this method, the simulation results are $v_0 = 46.9$ m/s, $v_1 = v_2 = 50.0$ m/s, and $v_3 = 24.1$ m/s, in Fig. 3 and 20.0 m/s for one single shift in Fig. 2. Benefitting from this strategy, the average velocity in long-range motion is increased to 42.75 m/s, which is two times larger than that of a single shift. In a shift device, the average velocity of long-range skyrmion motion is improved due to this improvement. In the following text, v_0 stands for the average velocity of the first shift in a long-range motion, and the maximum limit of long-range motion average velocity is defined as v_L . v_L is equal to $v_1(v_2)$ when the number of shifts increases.

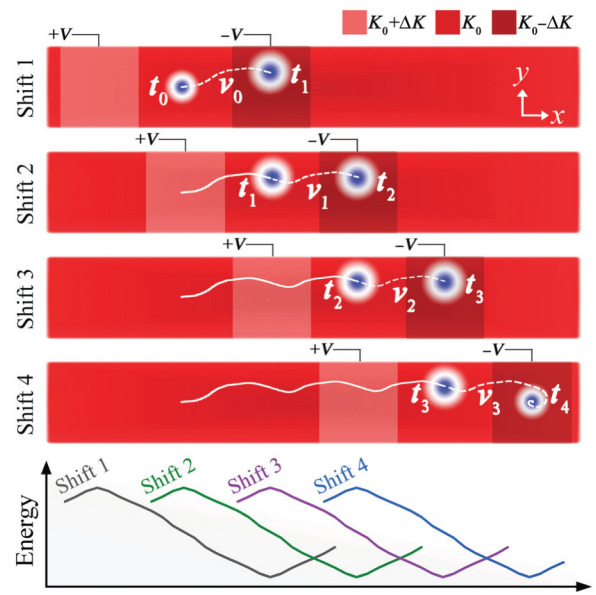


FIG. 3. Long-range motion trajectory and corresponding energy profiles for each shift. Energy wells move from left to right as the applied voltages switch from shift 1 to shift 4. To avoid the time-consuming procession, voltages are switched at the moments once the skyrmions pass the centers of the contacts. These moments are marked as t_1 to t_4 . v_0 , v_1 , v_2 , and v_3 are the average velocities of each shift, respectively. For the last shift, the voltage is on until the skyrmion is stabilized.

D. Velocity optimization

The magnetic parameters of K and D are tuned to optimize the performance of the voltage-driven skyrmion motion. In our simulation, the transverse drifts are strongly suppressed with the increase in D and a decrease in K . According to Eq. (4), the radii of skyrmions increase with the increase in D and decrease in K . Thus, the trajectory of a skyrmion's motion strongly depends on its radius.

The voltage-driven skyrmion motion benefits from the formation of an energy gradient when the nonuniform spin texture of a skyrmion crosses the boundaries of the contacts. To realize the energy gradient, the ratio of the skyrmion radius and the contact width, which is defined as l , should be optimized, as shown in Fig. 4(c). In the case of $2R_{\text{sk}} \ll l$, the skyrmion locates on an energy platform at its initial position and its motion is disabled. Because the spin texture is subject to the effective anisotropy field change based on $E = -\mathbf{m} \cdot \mathbf{H}$, the energy gradient in the range of $2R_{\text{sk}}$ can be formed only when the skyrmion enters or exits the contact boundaries. When the full texture of the skyrmion is located completely on the contact, the energy will not change with positions within the range of $l - 2R_{\text{sk}}$, (see the red curve in Appendix B Fig. 9). As the skyrmion size expands, the energy platform shrinks and the skyrmion starts to move since the energy gradient expands. When the skyrmion size fits $2R_{\text{sk}} = l$, the energy

platform completely disappears and the energy changes continually along the nanowire, which will promote high-efficiency skyrmion motion. With further expansion, the skyrmion size becomes larger than the contact width and hence, the energy platform shows up again. Considering an extreme case $R_{\text{sk}} \gg l$, the amount of spins located on the left and right contacts are approximately the same, thus the induced anisotropy energies in those two contacts with the positive and negative applied voltages cancel out each other and an energy platform forms. For the purpose of velocity optimization, we vary the skyrmion radius until it is half of the contact width, then the continually changing total energy along the nanowire is formed, and the ratio $2R_{\text{sk}}/l = 1$ is induced. By manipulating the device parameters D , K , and l , the initial average velocity v_0 increases until $2R_{\text{sk}}/l$ reaches 1, as shown in Fig. 4(d). As long as the damping constant α and the ratio $2R_{\text{sk}}/l$ are fixed, v_0 is roughly constant regardless of the values of D , K , and l , and the maximum v_0 is obtained when $2R_{\text{sk}}/l = 1$. This conclusion is verified by a developed analytical model to find the optimal contact width, where the contribution from the edge is ignored (see Appendix C). For a skyrmion with a 31-nm radius, the optimal contact width is found to be

58 nm, which is consistent with the OOMMF simulation results above.

By decreasing the damping constant, the velocity increases, which is consistent with Eq. (3). For a 1-nm Co-Fe-B layer, the typical damping constant varies in a wide range between 0.004 and 0.15 with different growth conditions and annealing treatments [66,67]. In our simulation, v_0 can reach 98.5 m/s under 0.3 V with $\alpha = 0.02$. Hence, higher velocity can be expected with a further decrease in α . Note that the nanowire with a 100-nm width limits the increase of the trajectory angle caused by the decrease in α .

In our designed structure for the voltage-driven skyrmion motion, the optimal velocity v_0 can be achieved when the skyrmion diameter ($2R_{\text{sk}}$) is equivalent to the contact width (l). Unlike v_0 , the initial stage for v_L is dynamic with an irregular skyrmion shape. Thus, v_L does not share the simple correlation with $2R_{\text{sk}}/l$ compared to that of v_0 .

Under the optimization of $2R_{\text{sk}}/l = 1$, the average velocity in the initial stage and long-range skyrmion motion are all simulated with different applied voltages and damping constants, as shown in Figs. 5(a) and 5(b).

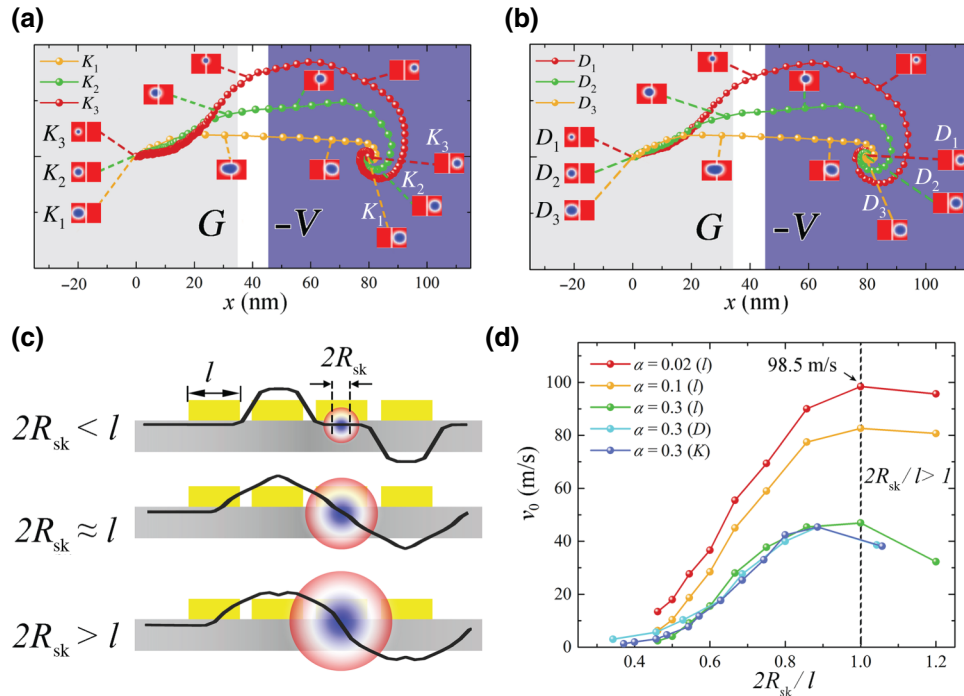


FIG. 4. (a) Skyrmion trajectories with different anisotropic constant K . $K_1 = 310$ kJ/m³, $K_2 = 335$ kJ/m³, and $K_3 = 360$ kJ/m³. DMI constant $D = 1.2$ mJ/m². (b) Skyrmion shift trajectories with different DMI constants D . $D_1 = 0.9$ mJ/m², $D_2 = 1.05$ mJ/m², and $D_3 = 1.2$ mJ/m². Anisotropic constant $K = 360$ kJ/m³. The shape and size of skyrmions at different moments during the shifts are simulated and presented by the insets in panels (a) and (b). The applied voltages for the left and right parts are ground and $-V$, respectively. (c) Side view and different energy profiles when skyrmion radius (R_{sk}) changes with a fixed contact width l . Energy platforms appear when R_{sk} is much less than $l/2$, and it disappears when $R_{\text{sk}} \approx l/2$. (d) The initial average velocity v_0 vs R_{sk}/l with different l . To realize the R_{sk}/l modulation, we change l , D , or K [49].

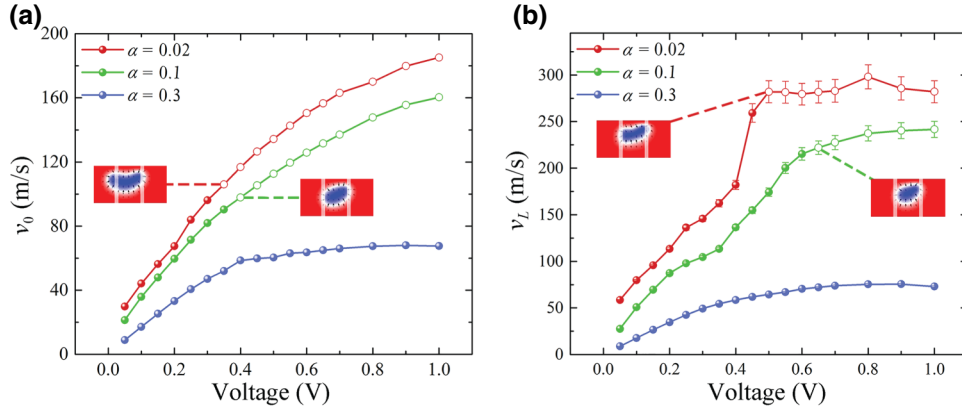


FIG. 5. (a) The initial average velocity v_0 . (b) The maximum limit of long-range motion average velocity v_L vs applied voltage V under different Gilbert damping constants α . Inserted images are simulated results of skyrmions indicating their size and shape at the moments when the center of the skyrmions passes the center of the contacts. For open symbols, the skyrmion diameter is calculated to be larger than contact with, i.e., $2R_{sk}/l > 1$, which is inapplicable to our device.

The average velocity increases with the increase in applied voltages and the decrease in damping constants. Nevertheless, a large applied voltage induces the skyrmion deformation, especially with a low damping constant as indicated in the insets of Figs. 5(a) and 5(b). The simulation data are marked as open dots when the large skyrmion deformation exceeds the contact size, which is not in consideration for effective data delivery. Therefore, for $\alpha = 0.02$, the maximum v_0 is limited to 98.5 m/s with 0.3 V and the maximum v_L is 259.3 m/s with 0.45 V (see Appendix D). For the long-range motion under 0.45 V, one shift costs only 0.27 ns, leading to a switching frequency of 3.7 GHz.

The energy cost is estimated in our designed structure, which is simply expressed as $E = 0.5CV^2$ for a single contact in one operation, where C is the device capacitance. When the contact width is fixed at 60 nm, C is set to be 0.37 fF, and the energy consumption is 8.4 aJ per operation at a 100-m/s velocity. To drive skyrmion motion under the same velocity, the voltage-driven method consumes three orders lower energy than that of the current-driven method [37,49,68].

III. CONCLUSION

In this work, we proposed a voltage-driven skyrmion motion method and numerically demonstrated its feasibility. Parameters are optimized with a model describing the skyrmion profile. In our system, the ratio of skyrmion diameter and voltage contact width is found to have a great impact on skyrmion velocity, which reaches its maximum value when the ratio equals 1. To overcome the problem of overshooting and relaxation in long-range skyrmion motion, we came up with the solution of raising the long-range velocity to 259 m/s with 0.45 V. Our concept can

be applied directly to the racetrack memory, with excellent characteristics such as low-power consumption, high storage density, and high switching frequency. In contrast to the current-driven method, the energy efficiency and addressable motion of the voltage-driven method show great advantages in the application of skyrmion-based spintronic applications.

ACKNOWLEDGMENTS

The authors gratefully acknowledge the National Natural Science Foundation of China (Grants No. 11574018, No. 61627813, No. 61571023, and No. 11574137), the International Collaboration Project B16001, and the National Key Technology Program of China Grant No. 2017ZX01032101 for their financial support of this work. X.Z. was supported by the Presidential Postdoctoral Fellowship of the Chinese University of Hong Kong, Shenzhen (CUHKSZ). Y.Z. acknowledges support by the President's Fund of CUHKSZ, and Shenzhen Fundamental Research Fund (Grants No. JCYJ20160331164412545 and No. JCYJ20170410171958839).

APPENDIX A: ANALYTICAL MODEL OF ENERGY EVOLUTION

To calculate the evolution of the total energy during skyrmion motion, we develop an analytical model to describe the energy change when different spin textures cross a step-like anisotropy profile, based on $E = -\mathbf{m} \cdot \mathbf{H}$. The anisotropic energy when the center of a domain structure arrives at x can be expressed as

$$E_{\text{ani}}(x) = \int_{\Omega} -\mathbf{m}(x) \cdot \mathbf{H} d\Omega, \quad (\text{A1})$$

where Ω stands for the integration interval (the whole nanowire) and \mathbf{H} is the effective field considering the VCMA effect, which only has a z component. The magnetic moment distribution in the nanowire is described by $\mathbf{m}(x)$, which changes with the spin texture motion. Once we know the analytical expression of the spin texture $\mathbf{m}(x)$, $E_{\text{ani}}(x)$ can be calculated numerically.

The energy evolutions during the motion for three different spin textures (uniform square domain, uniform circular domain, and skyrmion) are calculated, respectively. The domain structure moves along the x axis of a nanowire with finite width and infinite length. The boundary of the low- K region is set as $x = 0$, and the normalized analytical expression of \mathbf{H} is

$$H_z(x) = \begin{cases} -1, & \text{if } x \geq 0, \\ 0, & \text{if } x < 0, \end{cases} \quad (\text{A2})$$

where -1 stands for the normalized effective field induced by the VCMA effect.

First, we start the calculation from a uniform square domain with side lengths of a (blue and red arrows indicate spin-down and spin-up, respectively) as shown in Fig. 6. We let this domain structure move into the low- K region (dark gray region stands for the VCMA effect). The position of this square domain is described by its center $(x_{\text{rec}}, y_{\text{rec}})$. The analytical expression of $\mathbf{m}(x_{\text{rec}})$ just has a m_z component, written as

$$m_z(x_{\text{rec}}) = \begin{cases} -1, & \text{if } -\frac{a}{2} < x - x_{\text{rec}} < \frac{a}{2}, \\ 1, & \text{if else.} \end{cases} \quad (\text{A3})$$

In this case, the energy decreases linearly when the square spin-down structure crosses the boundary of the low- K region. The energy gradient linearly decreases in the region of a , which is the length of the spin-down domain structure, as shown in Fig. 6.

Second, we simulate the energy evolution when a uniform circular-shaped spin-down structure moves into the low- K region. The position of this circular shape domain is described by its center $(x_{\text{rec}}, y_{\text{rec}})$ and its radius is set as R . Similarly, the analytical expression of $\mathbf{m}(x_{\text{rec}})$ only has the m_z component, written as

$$m_z(x_{\text{rec}}) = \begin{cases} -1, & \text{if } (x - x_{\text{rec}})^2 + (y - y_{\text{rec}})^2 < R^2, \\ 1, & \text{if else.} \end{cases} \quad (\text{A4})$$

In this case, the energy is continually evaluated, but the energy gradient behavior is slightly different from that of the square spin-down structure, as shown in Fig. 7. The slope value of the energy gradient increases gradually when the spin-down domain starts to enter the low-

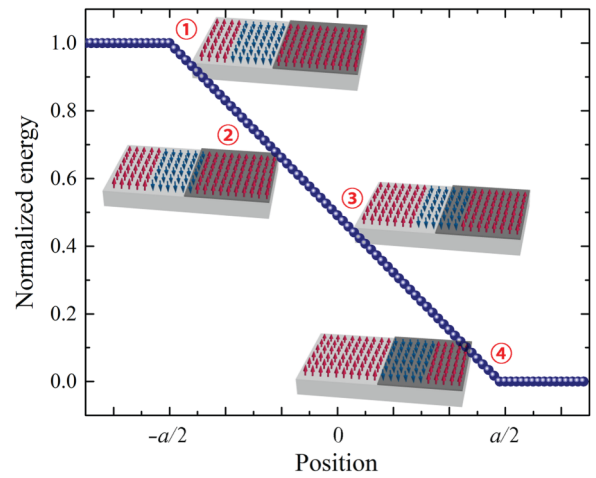


FIG. 6. The normalized energy profile along the wire when a uniform square spin texture moves into a low- K region (dark gray). Red and blue arrows stand for spin-up and spin-down moments, respectively.

K region, followed by an almost constant slope value, and then decreases gradually when the spin-down domain nearly enters the low- K region completely. The slight difference with the square shape domain above is from the amount of spin with a down direction due to the curved shape of the circle.

Finally, we simulate the energy evolution when a skyrmion moves into the low- K region. The position of the skyrmion is described by its center $(x_{\text{sk}}, y_{\text{sk}})$ and its radius is set as R_{sk} (radius of the $m_z = 0$ contour). An analytical model is deduced to describe the skyrmion texture. In a spherical coordinate system, magnetization at r is described by polar and azimuthal angles $\Theta(r, \phi)$ and

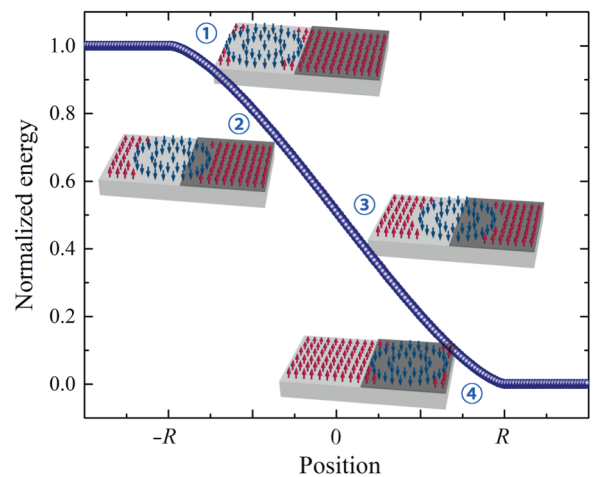


FIG. 7. The normalized energy profile along the wire when a uniform circular shape spin down moves into a low- K region (dark gray).

$\Phi(r, \phi)$. For a skyrmion centered at $r = 0$, the polar angle can be expressed as [21,69]

$$\Theta(r) = 2 \arctan \left[\frac{\sinh\left(\frac{R_{\text{sk}}}{w}\right)}{\sinh\left(\frac{r}{w}\right)} \right], \quad (\text{A5})$$

where w is the domain wall width. To apply this model in the rectangular coordinate system, the polar angle in the spherical coordinate $\Theta(r)$ is transformed to $\Theta(x, y)$ with the skyrmion centered at $(0, 0)$. The magnetic anisotropy energy when the skyrmion arrives at $(x_{\text{sk}}, y_{\text{sk}})$ can be expressed as

$$\begin{aligned} E_{\text{ani}}(x_{\text{sk}}) &= \int -\mathbf{m}(x_{\text{sk}}) \cdot \mathbf{H} d\Omega \\ &= \int -\cos[\Theta(x - x_{\text{sk}}, y - y_{\text{sk}})] \cdot |\mathbf{H}(x, y)| dx dy. \end{aligned} \quad (\text{A6})$$

In this case, the energy evolves continually and the energy gradient is different from that of the circular shape spin-down domain, as shown in Fig. 8. The energy almost does not change at the beginning and the energy gradient appears when the $m_z = 0$ contour crosses the low- K boundary. Due to the character of the skyrmion spin texture, the m_z is positive outside its radius ($m_z = 0$) and negative inside its radius in the skyrmion, while the amount of spin outside the radius is less than that inside the radius. Thus, the energy gradient can be negligible in the range outside of its radius ($-2R_{\text{sk}} \sim -R_{\text{sk}}$ and $R_{\text{sk}} \sim 2R_{\text{sk}}$), while the energy gradient obviously appears in the region from $-R_{\text{sk}}$ to R_{sk} .

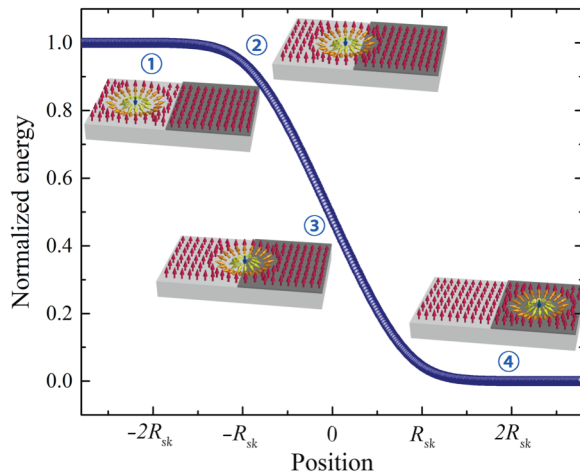


FIG. 8. The normalized energy profile along the wire when a skyrmion moves into a low- K region (Dark gray).

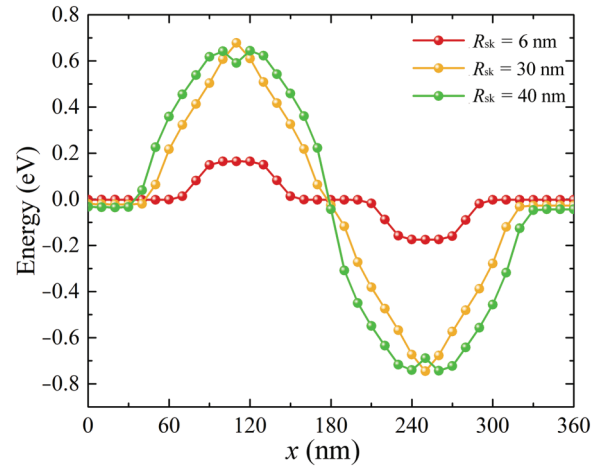


FIG. 9. The energy profile changes with different skyrmion radii. The contact width is fixed at 60 nm.

APPENDIX B: ENERGY PROFILE CHANGE WITH DIFFERENT SKYRMION RADIUS

In this part, we study the energy profile with varying the skyrmion radius R_{sk} . The voltage is applied as shown in Fig. 1 in the main text and the contact width l is fixed at 60 nm. As shown in Fig. 9, an energy platform appears in the energy profile when $2R_{\text{sk}} < l$ (red curve), and it disappears when $2R_{\text{sk}} \approx l$ (yellow curve), then reappears when $2R_{\text{sk}} > l$ (green curve). This change is consistent with the result in Appendix A that the energy gradient width depends on the relative skyrmion radius compared to the contact width.

APPENDIX C: OPTIMIZATION OF AVERAGE SHIFT VELOCITY

According to Eqs. (2) and (3) in the main text, the continuous change of E_{ani} generates the driving force F_g for the skyrmion motion, $F_g(x) = \partial_x E_{\text{ani}}(x)$. Assuming that the nanowire width is much larger than the skyrmion width, we ignore the force from the edge and the expression (3) for the x component can be simplified as

$$v_x(x) = \frac{F_{\text{grad}}(x)\alpha D_0}{G^2 + \alpha^2 D_0^2}. \quad (\text{C1})$$

We name the beginning and the destination of one skyrmion shift as x_0 and x_1 , respectively. From x to $x + dx$ in $[x_0, x_1]$, the time consumed can be estimated as $dt(x) = dx / \{[v_x(x) + v_x(x + dx)]/2\}$. Therefore, the total time consumed in this shift is the integration of $dt(x)$ for x in $[x_0, x_1]$ and the average velocity of this shift can be expressed as $v = [(x_1 - x_0) / \int_{x_0}^{x_1} dt(x)]$. Based on the energy profile calculated in Appendix A, the average velocity can be calculated with different widths of contact. Ignoring the spacing between the contacts and the

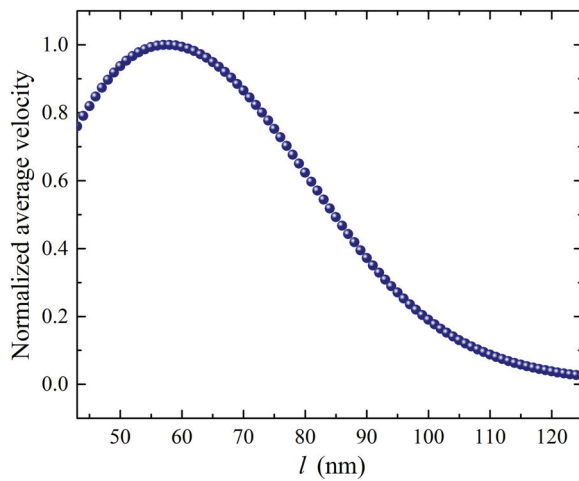
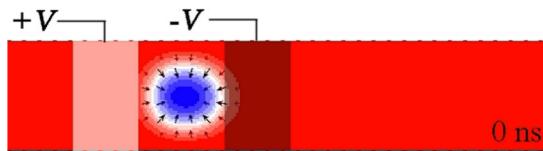


FIG. 10. The normalized average velocity changes with different contact widths l .

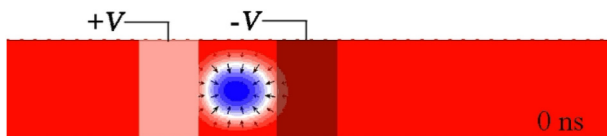
skymion size change during the shift, the average velocity is calculated when varying the width of the contact with a fixed skymion radius of 31 nm ($K = 310$ kJ/m³, $D = 1.2$ mJ/m²). The numerical result in Fig. 10 reveals that the maximum of the average velocity is obtained when the contact width l is 58 nm, which is about twice that of the skymion radius R_{sk} . This conclusion is coherent with the result in Appendix B, as the energy platform will decrease the motion velocity.

APPENDIX D: VIDEOS OF SKYRMION MOTION

Two voltage-driven motion videos are attached. Both of them contain three shifts. Videos 1 and 2 are the skymion motion driven by voltages under 0.3 V with $\alpha = 0.1$ and 0.45 V with $\alpha = 0.02$, where the average velocities are about 100 and 249 m/s, respectively.



VIDEO 1. The skymion motion under 0.3 V with damping of 0.1 and the velocity reaches 100 m/s.



VIDEO 2. The skymion motion under 0.45 V with damping of 0.02 and the velocity reaches 249 m/s.

- [1] A. Fert, V. Cros, and J. Sampaio, Skymions on the track, *Nat. Nanotechnol.* **8**, 152 (2013).
- [2] R. Tomasello, E. Martinez, R. Zivieri, L. Torres, M. Carpentieri, and G. Finocchio, A strategy for the design of skymion racetrack memories, *Sci. Rep.* **4**, 6784 (2015).
- [3] W. Koshibae, Y. Kaneko, J. Iwasaki, M. Kawasaki, Y. Tokura, and N. Nagaosa, Memory functions of magnetic skymions, *Jpn. J. Appl. Phys.* **54**, 53001 (2015).
- [4] G. Yu, P. Upadhyaya, Q. Shao, H. Wu, G. Yin, X. Li, C. He, W. Jiang, X. Han, P. K. Amiri, and K. L. Wang, Room-temperature skymion shift device for memory application, *Nano Lett.* **17**, 261 (2017).
- [5] Y. Zhou and M. Ezawa, A reversible conversion between a skymion and a domain-wall pair in a junction geometry, *Nat. Commun.* **5**, 1 (2014).
- [6] W. Kang, Y. Huang, X. Zhang, Y. Zhou, and W. Zhao, Skymion-electronics: an overview and outlook, *Proc. IEEE* **104**, 2040 (2016).
- [7] W. Jiang, W. Zhang, G. Yu, M. B. Jungfleisch, P. Upadhyaya, H. Somaily, J. E. Pearson, Y. Tserkovnyak, K. L. Wang, O. Heinonen, S. G. E. te Velthuis, and A. Hoffmann, Mobile Néel skymions at room temperature: Status and future, *AIP Adv.* **6**, 55602 (2016).
- [8] S. Rohart and A. Thiaville, Skymion confinement in ultrathin film nanostructures in the presence of Dzyaloshinskii-Moriya interaction, *Phys. Rev. B* **88**, 184422 (2013).
- [9] X. Zhang, J. Müller, J. Xia, M. Garst, X. Liu, and Y. Zhou, Motion of skymions in nanowires driven by magnonic momentum-transfer forces, *New J. Phys.* **19**, 065001 (2017).
- [10] L. Sun, R. X. Cao, B. F. Miao, Z. Feng, B. You, D. Wu, W. Zhang, A. Hu, and H. F. Ding, Creating an Artificial Two-Dimensional Skymion Crystal by Nanopatterning, *Phys. Rev. Lett.* **110**, 167201 (2013).
- [11] L. Kong and J. Zang, Dynamics of an Insulating Skymion under a Temperature Gradient, *Phys. Rev. Lett.* **111**, 067203 (2013).
- [12] W. Koshibae and N. Nagaosa, Creation of skymions and antiskymions by local heating, *Nat. Commun.* **5**, 5148 (2014).
- [13] Z. Li, Y. Zhang, Y. Huang, C. Wang, X. Zhang, Y. Liu, Y. Zhou, W. Kang, S. C. Koli, and N. Lei, Strain-controlled skymion creation and propagation in ferroelectric/ferromagnetic hybrid wires, *J. Magn. Magn. Mater.* **455**, 19 (2018).
- [14] C. Wang, D. Xiao, X. Chen, Y. Zhou, and Y. Liu, Manipulating and trapping skymions by magnetic field gradients, *New J. Phys.* **19**, 83008 (2017).
- [15] Y. Huang, W. Kang, X. Zhang, Y. Zhou, and W. Zhao, Magnetic skymion-based synaptic devices, *Nanotechnology* **28**, 08LT02 (2017).
- [16] S. Seki, X. Z. Yu, S. Ishiwata, and Y. Tokura, Observation of skymions in a multiferroic material, *Science* **336**, 198 (2012).
- [17] O. Boulle, J. Vogel, H. Yang, S. Pizzini, D. De Souza Chaves, A. Locatelli, T. O. Menteş, A. Sala, L. D. Buda-Prejbeanu, O. Klein, M. Belmeguenai, Y. Roussigné,

- A. Stashkevich, S. Mourad Chérif, L. Aballe, M. Foerster, M. Chshiev, S. Auffret, I. M. Miron, and G. Gaudin, Room-temperature chiral magnetic skyrmions in ultrathin magnetic nanostructures, *Nat. Nanotechnol.* **11**, 449 (2016).
- [18] Y. Onose, Y. Okamura, S. Seki, S. Ishiwata, and Y. Tokura, Observation of Magnetic Excitations of Skyrmion Crystal in a Helimagnetic Insulator Cu_2OSeO_3 , *Phys. Rev. Lett.* **109**, 037603 (2012).
- [19] M. Mochizuki, X. Z. Yu, S. Seki, N. Kanazawa, W. Koshibae, J. Zang, M. Mostovoy, Y. Tokura, and N. Nagaosa, Thermally driven ratchet motion of a skyrmion microcrystal and topological magnon Hall effect, *Nat. Mater.* **13**, 241 (2014).
- [20] K. Shibata, X. Z. Yu, T. Hara, D. Morikawa, N. Kanazawa, K. Kimoto, S. Ishiwata, Y. Matsui, and Y. Tokura, Towards control of the size and helicity of skyrmions in helimagnetic alloys by spin-orbit coupling, *Nat. Nanotechnol.* **8**, 723 (2013).
- [21] N. Romming, A. Kubetzka, C. Hanneken, K. von Bergmann, and R. Wiesendanger, Field-Dependent Size and Shape of Single Magnetic Skyrmions, *Phys. Rev. Lett.* **114**, 177203 (2015).
- [22] J. S. White, I. Levatić, A. A. Omrani, N. Egetenmeyer, K. Prša, I. Živković, J. L. Gavilano, J. Kohlbrecher, M. Bartkowiak, H. Berger, and H. M. Rønnow, Electric field control of the skyrmion lattice in Cu_2OSeO_3 , *J. Phys.: Condens. Matter* **24**, 432201 (2012).
- [23] M. Finazzi, M. Savoini, A. R. Khorsand, A. Tsukamoto, A. Itoh, L. Duò, A. Kirilyuk, T. Rasing, and M. Ezawa, Laser-Induced Magnetic Nanostructures with Tunable Topological Properties, *Phys. Rev. Lett.* **110**, 177205 (2013).
- [24] S.-Z. Lin, C. D. Batista, C. Reichhardt, and A. Saxena, Ac Current Generation in Chiral Magnetic Insulators and Skyrmion Motion Induced by the Spin Seebeck Effect, *Phys. Rev. Lett.* **112**, 187203 (2014).
- [25] M. Schott, A. Bernand-Mantel, L. Ranno, S. Pizzini, J. Vogel, H. Béa, C. Baraduc, S. Auffret, G. Gaudin, and D. Givord, The skyrmion switch: Turning magnetic skyrmion bubbles on and off with an electric field, *Nano Lett.* **17**, 3006 (2017).
- [26] F. Jonietz, S. Mühlbauer, C. Pfleiderer, A. Neubauer, W. Münzer, A. Bauer, T. Adams, R. Georgii, P. Boni, R. A. Duine, K. Everschor, M. Garst, and A. Rosch, Spin transfer torques in MnSi at ultralow current densities, *Science* **330**, 1648 (2010).
- [27] N. Romming, C. Hanneken, M. Menzel, J. E. Bickel, B. Wolter, K. von Bergmann, A. Kubetzka, and R. Wiesendanger, Writing and deleting single magnetic skyrmions, *Science* **341**, 636 (2013).
- [28] K. Everschor, M. Garst, B. Binz, F. Jonietz, S. Mühlbauer, C. Pfleiderer, and A. Rosch, Rotating skyrmion lattices by spin torques and field or temperature gradients, *Phys. Rev. B* **86**, 054432 (2012).
- [29] F. Büttner, I. Lemesch, M. Schneider, B. Pfau, C. M. Günther, P. Hessler, J. Geilhufe, L. Caretta, D. Engel, B. Krüger, J. Viehhaus, S. Eisebitt, and G. S. D. Beach, Field-free deterministic ultrafast creation of magnetic skyrmions by spin-orbit torques, *Nat. Nanotechnol.* **12**, 1040 (2017).
- [30] W. Legrand, D. Maccariello, N. Reyren, K. Garcia, C. Moutafis, C. Moreau-Luchaire, S. Collin, K. Bouzouhane, V. Cros, and A. Fert, Room-temperature current-induced generation and motion of sub-100 nm skyrmions, *Nano Lett.* **17**, 2703 (2017).
- [31] J. Iwasaki, M. Mochizuki, and N. Nagaosa, Current-induced skyrmion dynamics in constricted geometries, *Nat. Nanotechnol.* **8**, 742 (2013).
- [32] J. Zang, M. Mostovoy, J. H. Han, and N. Nagaosa, Dynamics of Skyrmion Crystals in Metallic Thin Films, *Phys. Rev. Lett.* **107**, 136804 (2011).
- [33] J. Iwasaki, W. Koshibae, and N. Nagaosa, Colossal spin transfer torque effect on skyrmion along the edge, *Nano Lett.* **14**, 4432 (2014).
- [34] T. Schulz, R. Ritz, A. Bauer, M. Halder, M. Wagner, C. Franz, C. Pfleiderer, K. Everschor, M. Garst, and A. Rosch, Emergent electrodynamics of skyrmions in a chiral magnet, *Nat. Phys.* **8**, 301 (2012).
- [35] X. Z. Yu, N. Kanazawa, W. Z. Zhang, T. Nagai, T. Hara, K. Kimoto, Y. Matsui, Y. Onose, and Y. Tokura, Skyrmion flow near room temperature in an ultralow current density, *Nat. Commun.* **3**, 988 (2012).
- [36] W. Jiang, P. Upadhyaya, W. Zhang, G. Yu, M. B. Jungfleisch, F. Y. Fradin, J. E. Pearson, Y. Tserkovnyak, K. L. Wang, O. Heinonen, S. G. E. Te Velthuis, and A. Hoffmann, Blowing magnetic skyrmion bubbles, *Science* **349**, 283 (2015).
- [37] S. Woo, K. Litzius, B. Krüger, M.-Y. Im, L. Caretta, K. Richter, M. Mann, A. Krone, R. M. Reeve, M. Weigand, P. Agrawal, I. Lemesch, M.-A. Mawass, P. Fischer, M. Kläui, and G. S. D. Beach, Observation of room-temperature magnetic skyrmions and their current-driven dynamics in ultrathin metallic ferromagnets, *Nat. Mater.* **15**, 501 (2016).
- [38] G. Yu, P. Upadhyaya, X. Li, W. Li, S. K. Kim, Y. Fan, K. L. Wong, Y. Tserkovnyak, P. K. Amiri, and K. L. Wang, Room-temperature creation and spin-orbit torque manipulation of skyrmions in thin films with engineered asymmetry, *Nano Lett.* **16**, 1981 (2016).
- [39] H. T. Fook, W. L. Gan, and W. S. Lew, Gateable skyrmion transport via field-induced potential barrier modulation, *Sci. Rep.* **6**, 21099 (2016).
- [40] J. Müller and A. Rosch, Capturing of a magnetic skyrmion with a hole, *Phys. Rev. B* **91**, 054410 (2015).
- [41] W. Kang, Y. Huang, C. Zheng, W. Lv, N. Lei, Y. Zhang, X. Zhang, Y. Zhou, and W. Zhao, Voltage controlled magnetic skyrmion motion for racetrack memory, *Sci. Rep.* **6**, 23164 (2016).
- [42] H. Ohno, D. Chiba, F. Matsukura, T. Omiya, E. Abe, T. Dietl, Y. Ohno, and K. Ohtani, Electric-field control of ferromagnetism, *Nature* **408**, 944 (2000).
- [43] H. Ohno, A window on the future of spintronics, *Nat. Mater.* **9**, 952 (2010).
- [44] P.-J. Hsu, A. Kubetzka, A. Finco, N. Romming, K. von Bergmann, and R. Wiesendanger, Electric-field-driven switching of individual magnetic skyrmions, *Nat. Nanotechnol.* **12**, 123 (2016).
- [45] C. Ma, X. Zhang, J. Xia, M. Ezawa, W. Jiang, T. Ono, S. N. Piramanayagam, A. Morisako, Y. Zhou, and X. Liu, Electric field-induced creation and directional motion of

- domain walls and skyrmion bubbles, *Nano Lett.* (to be published).
- [46] X. Wang, W. L. Gan, J. C. Martinez, F. N. Tan, M. B. A. Jalil, and W. S. Lew, Efficient skyrmion transport mediated by a voltage controlled magnetic anisotropy gradient, *Nanoscale* **10**, 733 (2018).
- [47] S. Ikeda, K. Miura, H. Yamamoto, K. Mizunuma, H. D. Gan, M. Endo, S. Kanai, J. Hayakawa, F. Matsukura, and H. Ohno, A perpendicular-anisotropy CoFeB-MgO magnetic tunnel junction, *Nat. Mater.* **9**, 721 (2010).
- [48] J. Torrejon, J. Kim, J. Sinha, S. Mitani, M. Hayashi, M. Yamanouchi, and H. Ohno, Interface control of the magnetic chirality in CoFeB/MgO heterostructures with heavy-metal underlayers, *Nat. Commun.* **5**, 1 (2014).
- [49] See Supplemental Material at <http://link.aps.org/supplemental/10.1103/PhysRevApplied.11.014004> for the detailed discussion of K_{edge} , magnetic parameters and energy consumption.
- [50] H. T. Fook, W. L. Gan, I. Purnama, and W. S. Lew, Mitigation of magnus force in current-induced skyrmion dynamics, *IEEE Trans. Magn.* **51**, 1500204 (2015).
- [51] P. Lai, G. P. Zhao, H. Tang, N. Ran, S. Q. Wu, J. X. X. Zhang, and Y. Zhou, An Improved racetrack structure for transporting a skyrmion, *Sci. Rep.* **7**, 45330 (2015).
- [52] T. Devolder, I. Barisic, S. Eimer, K. Garcia, J.-P. Adam, B. Ockert, and D. Ravelosona, Irradiation-induced tailoring of the magnetism of CoFeB/MgO ultrathin films, *J. Appl. Phys.* **113**, 203912 (2013).
- [53] T. Jin, F. Tan, W. C. Law, W. Gan, I. Soldatov, R. Schäfer, C. Ma, X. Liu, W. S. Lew, and S. N. Piramanayagam, Nanoscale modification of magnetic properties for effective domain wall pinning, *J. Magn. Magn. Mater.* **475**, 70 (2019).
- [54] W.-G. Wang, M. Li, S. Hageman, and C. L. Chien, Electric-field-assisted switching in magnetic tunnel junctions, *Nat. Mater.* **11**, 64 (2012).
- [55] Y. Shiota, T. Nozaki, F. Bonell, S. Murakami, T. Shinjo, and Y. Suzuki, Induction of coherent magnetization switching in a few atomic layers of FeCo using voltage pulses, *Nat. Mater.* **11**, 39 (2012).
- [56] S. Kanai, M. Yamanouchi, S. Ikeda, Y. Nakatani, F. Matsukura, and H. Ohno, Electric field-induced magnetization reversal in a perpendicular-anisotropy CoFeB-MgO magnetic tunnel junction, *Appl. Phys. Lett.* **101**, 122403 (2012).
- [57] W. Skowroński, T. Nozaki, Y. Shiota, S. Tamaru, K. Yakushiji, H. Kubota, A. Fukushima, S. Yuasa, and Y. Suzuki, Perpendicular magnetic anisotropy of Ir/CoFeB/MgO trilayer system tuned by electric fields, *Appl. Phys. Express* **8**, 53003 (2015).
- [58] X. Li, K. Fitzell, D. Wu, C. T. Karaba, A. Buditama, G. Yu, K. L. Wong, N. Altieri, C. Grezes, N. Kioussis, S. Tolbert, Z. Zhang, J. P. Chang, P. Khalili Amiri, and K. L. Wang, Enhancement of voltage-controlled magnetic anisotropy through precise control of Mg insertion thickness at CoFeB/MgO interface, *Appl. Phys. Lett.* **110**, 52401 (2017).
- [59] T. Nozaki, A. Koziol-Rachwał, W. Skowronski, V. Zayets, Y. Shiota, S. Tamaru, H. Kubota, A. Fukushima, S. Yuasa, and Y. Suzuki, Large Voltage-Induced Changes in the Perpendicular Magnetic Anisotropy of an MgO-Based Tunnel Junction with an Ultrathin Fe Layer, *Phys. Rev. Appl.* **5**, 044006 (2016).
- [60] A. Koziol-Rachwał, T. Nozaki, K. Freindl, J. Korecki, S. Yuasa, and Y. Suzuki, Enhancement of perpendicular magnetic anisotropy and its electric field-induced change through interface engineering in Cr/Fe/MgO, *Sci. Rep.* **7**, 5993 (2017).
- [61] S. Peng, M. Wang, H. Yang, L. Zeng, J. Nan, J. Zhou, Y. Zhang, A. Hallal, M. Chshiev, K. L. Wang, Q. Zhang, and W. Zhao, Origin of interfacial perpendicular magnetic anisotropy in MgO/CoFe/metallic capping layer structures, *Sci. Rep.* **5**, 18173 (2016).
- [62] D. V. Dimitrov, Z. Gao, X. Wang, W. Jung, X. Lou, and O. G. Heinonen, Dielectric breakdown of MgO magnetic tunnel junctions, *Appl. Phys. Lett.* **94**, 123110 (2009).
- [63] Y. Zhang, X. Lin, J.-P. Adam, G. Agnus, W. Kang, W. Cai, J.-R. Coudeville, N. Isac, J. Yang, H. Yang, K. Cao, H. Cui, D. Zhang, Y. Zhang, C. Zhao, W. Zhao, and D. Ravelosona, Heterogeneous memristive devices enabled by magnetic tunnel junction nanopillars surrounded by resistive silicon switches, *Adv. Electron. Mater.* **4**, 1700461 (2018).
- [64] A. A. Thiele, Steady-State Motion of Magnetic Domains, *Phys. Rev. Lett.* **30**, 230 (1973).
- [65] A. Thiaville, Y. Nakatani, J. Miltat, and Y. Suzuki, Micro-magnetic understanding of current-driven domain wall motion in patterned nanowires, *Europhys. Lett.* **69**, 990 (2005).
- [66] X. Liu, W. Zhang, M. J. Carter, and G. Xiao, Ferromagnetic resonance and damping properties of CoFeB thin films as free layers in MgO-based magnetic tunnel junctions, *J. Appl. Phys.* **110**, 33910 (2011).
- [67] S. Iihama, Q. Ma, T. Kubota, S. Mizukami, Y. Ando, and T. Miyazaki, Damping of magnetization precession in perpendicularly magnetized CoFeB alloy thin films, *Appl. Phys. Express* **5**, 83001 (2012).
- [68] A. Fert, N. Reyren, and V. Cros, Magnetic skyrmions: Advances in physics and potential applications, *Nat. Rev. Mater.* **2**, 17031 (2017).
- [69] X. S. Wang, H. Y. Yuan, and X. R. Wang, A theory on skyrmion size, *Commun. Phys.* **1**, 31 (2018).